Abiotic Pyrite Formation Produces a Large Fe Isotope Fractionation

Authors' final draft or 'Post-Print' version. The final version was accepted for publication in Science and published by the American Association for the Advancement of Science (2012).

Cite as: Guilbaud, R, Butler, IB & Ellam, RM 2011, 'Abiotic Pyrite Formation Produces a Large Fe Isotope Fractionation' *Science*, vol 332, no. 6037, pp. 1548-1551.

DOI: 10.1126/science.1202924

Abiotic pyrite formation produces a large Fe isotope fractionation

Romain Guilbaud,[1,2,*] Ian B. Butler,[1,2] Rob M. Ellam[3,2]

[1]School of Geosciences, University of Edinburgh, Grant Institute, Edinburgh EH9 3JW, UK, [2]Scottish Universities Environmental Research Centre, Rankine Avenue, East Kilbride G75 0QF, UK,

[3]ECOSSE (Edinburgh Collaborative of Subsurface Science and Engineering), A Joint Research Institute of the Edinburgh Research Partnership in Engineering and Mathematics.

[*]e-mail: R.Guilbaud@sms.ed.ac.uk

The iron isotope composition of sedimentary pyrite has been proposed as a potential proxy to trace microbial metabolism and the redox evolution of the oceans. Here, we demonstrate that Fe isotope fractionation accompanies abiotic pyrite formation in the absence of Fe(II) redox change. Combined fractionation factors between $Fe(II)_{aq}$, mackinawite and pyrite permit the generation of pyrite with Fe isotope signatures that nearly encapsulate the full range of sedimentary $\delta^{56}Fe_{pyrite}$ recorded in both Archean and modern sediments. We propose that Archean negative Fe isotope excursions reflect a small extent of $Fe(II)_{aq}$ utilization rather than microbial dissimilatory Fe(III) reduction. Late Proterozoic to modern sediments may reflect higher extent of $Fe(II)_{aq}$ utilization and variations in source composition.

The analysis and interpretation of textural, compositional and isotopic signatures contained within sedimentary pyrite (FeS_2) inform debate concerning models for the evolution of Earth's ocean and atmosphere system. Over the last decade, growing interest in Fe isotopes as biogeochemical tracers has led to the collection of a spectrum of data which illustrates the variation of $\delta^{56}Fe$ for sedimentary pyrite throughout Earth's history, ranging between $\delta^{56}Fe$ ~ +0.2 to -1 ‰ in the Phanerozoic and +1.2 to -3.5 ‰ in the Paleoproterozoic and Archean *(1, 2)*. In modern anoxic basins, diagenetic pyrite displays isotopic compositions of between -0.4 and -1.2 ‰ *(3)*.

Detailed interpretations of the fluctuating secular $\delta^{56}Fe_{pyrite}$ trends are still debated because natural data are far from theoretical computations that predict an equilibrium fractionation $\Delta^{56}Fe_{Fe(II)\text{-}pyrite}$ varying from ~ -2.5 to -4.5 ‰, with pyrite being ^{56}Fe enriched *(4)*. On mixing $Fe(II)_{aq}$ and $S(-II)_{aq}$, the first phase to precipitate, mackinawite (FeS_m), incorporates lighter isotopes, recording a kinetic fractionation $\Delta^{56}Fe_{Fe(II)\text{-}FeS}$ varying from +0.9 ‰ to +0.3 ‰ *(5)*, and it has been proposed that sedimentary pyrite formation should record a fractionation similar to $\Delta^{56}Fe_{Fe(II)\text{-}FeS}$ *(1, 4, 6)*. This implies that a mechanism is required to produce ^{56}Fe isotope excursions more negative than -1 ‰ as recorded in Archean sedimentary rocks. Dissimilatory iron(III) reduction (DIR) – an important anoxic metabolic pathway – can produce large amounts of ^{56}Fe depleted $Fe(II)_{aq}$ and it has been proposed that the large Fe isotope variations observed in Precambrian sedimentary pyrite and banded iron formations (BIFs) are evidence for widespread DIR *(7)*. This potential microbial origin for the ^{56}Fe depletion of Archean pyrite has been supported by co-variations in Fe and S isotopes *(8)*. However, such large variations in $\delta^{56}Fe$ have not been identified in modern anoxic sediments, where these microbial processes are substantial *(3, 9)*. Because abiotic $Fe(II)_{aq}$ oxidation also produces large fractionations where residual $Fe(II)_{aq}$ is ^{56}Fe depleted *(10)* redox effects have been proposed as an alternative explanation for Paleoproterozoic and Archean $\delta^{56}Fe_{pyrite}$ *(2)*. Fe removal as Fe

(oxy)hydroxides and BIFs precursor minerals would preferentially incorporate ^{56}Fe *(2, 11)* and subsequent sulfide precipitation would reflect the ^{56}Fe depleted $Fe(II)_{aq}$. Interestingly, both of these models are predicated on the hypothesis that pyrite is a passive recorder of the $Fe(II)_{aq}$ pool. The assumption is that an isotopically light Fe reservoir is the essential ingredient to produce isotopically light pyrite.

We report experimentally derived Fe isotope fractionation factors for abiotic pyrite formation at 40°C and 100°C at pH 6 *(12)*. Pyrite was synthesized under anoxic conditions via the H_2S pathway *(13)* where FeS_m (initial $\delta^{56}Fe_{FeS}$ was +0.3 ‰) dissolves to form aqueous FeS clusters (FeS^0_{aq}) which react with H_2S to form pyrite. Pyrite was separated from its Fe(II) reservoir ($Fe(II)_{RES} = FeS_m + FeS^0_{aq}$) and the isotopic compositions of pyrite and $Fe(II)_{RES}$ were measured. At 40°C and 100°C, the abiotic fractionation $\Delta^{56}Fe_{Fe(II)RES\text{-}pyrite}$ varies from +1.7 to +3.0 ‰ ± 0.1 ‰ (~2.2 ‰ on average) (Fig. 1a). Isotopic mass balance for each experiment (Table S1) and replicate analysis indicate that the experimental error is small and our results are reproducible. The kinetic fractionation factors ($\alpha'_{Fe(II)RES\text{-}pyrite}$) are 1.0025 ± 0.0007 and 1.0021 ± 0.0004 at 40°C and 100°C, respectively. Within errors, these fractionation factors are indistinguishable and on average $\alpha'_{Fe(II)RES\text{-}pyrite} = 1.0022 \pm 0.0007$. This is large compared to the fractionation during FeS_m formation. We measured maximum rates of pyrite formation (~2.8×10^{-6} mol pyrite l^{-1} s^{-1}) close to published data [~ 3×10^{-6} mol pyrite l^{-1} s^{-1}, *(13)*]. The pyrite forming process is mechanistically uniform over the 25°C-125°C temperature range *(13)*, and the observed temperature independent effect indicates that our results may be extrapolated with reasonable confidence to ambient temperatures. The potential Fe isotope effect associated with FeS_m dissolution into FeS^0_{aq} is unknown, but should be small because FeS_m and FeS^0_{aq} are structurally congruent *(14)*. This means that measured $\Delta^{56}Fe_{Fe(II)RES\text{-}pyrite}$ approximates $\Delta^{56}Fe_{FeSm\text{-}pyrite}$ and $\Delta^{56}Fe_{FeS(0)aq\text{-}pyrite}$.

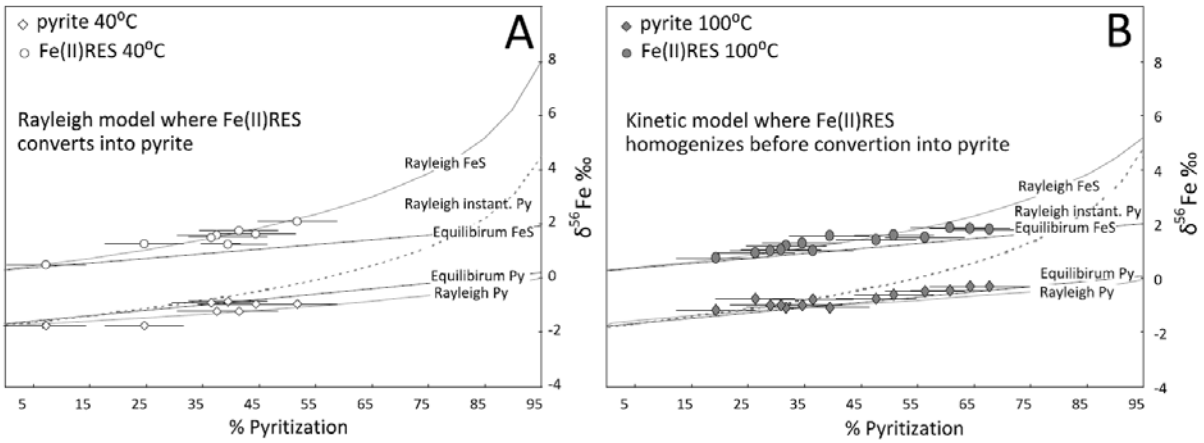

Fig. 1: Results for 40°C (A, white symbols) and 100°C (B, gray symbols) experiments. Circles and diamonds represent $Fe(II)_{RES}$ and pyrite, respectively. Bold lines represent a putative isotope equilibrium evolution. Dashed lines ("Rayleigh instant. Py") represent the composition of neoformed pyrite at every time, and the bulk compositions of pyrite and $Fe(II)_{RES}$ evolve along the light curves. Both datasets fit a kinetic model (Rayleigh model, light curves). At 40°C, $Fe(II)_{RES}$ evolves more quickly towards ^{56}Fe enriched values since FeS^0_{aq} - from which pyrite precipitates - gets more and more ^{56}Fe enriched without equilibration with FeS_m. At 100°C, FeS_m and FeS^0_{aq}, are allowed to equilibrate before transferring into pyrite, therefore $Fe(II)_{RES}$ evolves more slowly towards ^{56}Fe enriched values.

$\delta^{56}Fe$ values for $Fe(II)_{RES}$ and pyrite fit with a simple Rayleigh model for the experiments carried out at 40°C (Fig. 1a). In this model, $Fe(II)_{RES}$ is progressively converted into pyrite in a closed system. At 100°C (Fig. 1b), the system apparently evolves along an isotopically equilibrated pathway. Pyrite is very sparingly soluble *(15)*, and pyrite formation is effectively a unidirectional reaction; thus the associated fractionation is very unlikely to reflect isotopic exchange equilibrium. Fig. 1b shows a Rayleigh model that allows continuous FeS_m-FeS^0_{aq} equilibration within the reservoir during pyrite precipitation. The model suggests that our data can be reproduced using a unidirectional, multistep pathway, and that isotopic equilibrium is only apparent. Consequently our experimentally determined results differ considerably from theoretical computations that predict ^{56}Fe enrichment in pyrite at equilibrium *(4)*. The fractionation recorded here is large compared to other reactions that do not involve any redox change for Fe(II) atoms *(5)*. Although there is no redox change for Fe(II) during pyrite formation, there is a shift from Fe(II) in a tetrahedrally coordinated high spin d^6 configuration in FeS^0_{aq} to Fe(II) in an octahedrally coordinated low spin d^6 configuration in pyrite

(15). Preferential incorporation of ^{56}Fe depleted Fe(II) into pyrite may be related to selection during this change of coordination and spin state *(16)* during pyrite formation. Abiotic Fe isotope fractionations induced by changes in geometry have been previously proposed *(17)* but it is not clear if this is the case for Fe sulfides.

In most sedimentary environments, the H_2S pathway is the dominant pyrite forming mechanism since polysulfide is a minor $S(-II)_{aq}$ species relative to H_2S_{aq} under the entire oceanic pH range *(15)*. Polysulfides may be more important at the oxic/anoxic interface (e.g. at the surface of Fe(III) oxyhydroxides) under alkaline conditions and the polysulfide pathway may nucleate pyrite. Further pyrite formation however, would involve H_2S and bulk pyrite signatures reflect the H_2S pathway *(18)*. The role of FeS_m as a reactant for pyrite formation may have been particularly important in Proterozoic and Archean oceans, which were characterized by high $Fe(II)_{aq}$ concentrations *(19)*. In anoxic Archean oceans, the precipitation of iron sulfides was restricted to regions where bacterial sulfate was actively producing S(-II). Assuming continuous hydrothermal $Fe(II)_{aq}$ inputs with an isotopic composition ~ 0 ‰ *(7, 20)*, Fe(II) would be partly removed from solution as FeS_m isotopic compositions varying from -0.9 to -0.3 ‰ *(5)*. FeS_m dissolution to FeS^0_{aq} and isotope exchange between FeS^0_{aq} and $Fe(II)_{aq}$ would produce a range of isotopic compositions varying from -0.9 to +0.5 ‰ for FeS^0_{aq} *(5, 21)*. Subject to the rate and the extent of Fe utilization, subsequent pyrite would record isotopic compositions from ~ -3.1 to + 0.5 ‰ (Fig. 2). This means that combining our result for $\Delta^{56}Fe_{FeS(0)aq\text{-}pyrite}$ with kinetic and equilibrium Fe isotope fractionation between $Fe(II)_{aq}$ and FeS_m, almost the entire range of natural pyrite compositions falls within the range of possible compositions generated by the abiological pyrite formation process itself. Thus Archean and Proterozoic Fe isotope excursions need not reflect particular redox or DIR contributions.

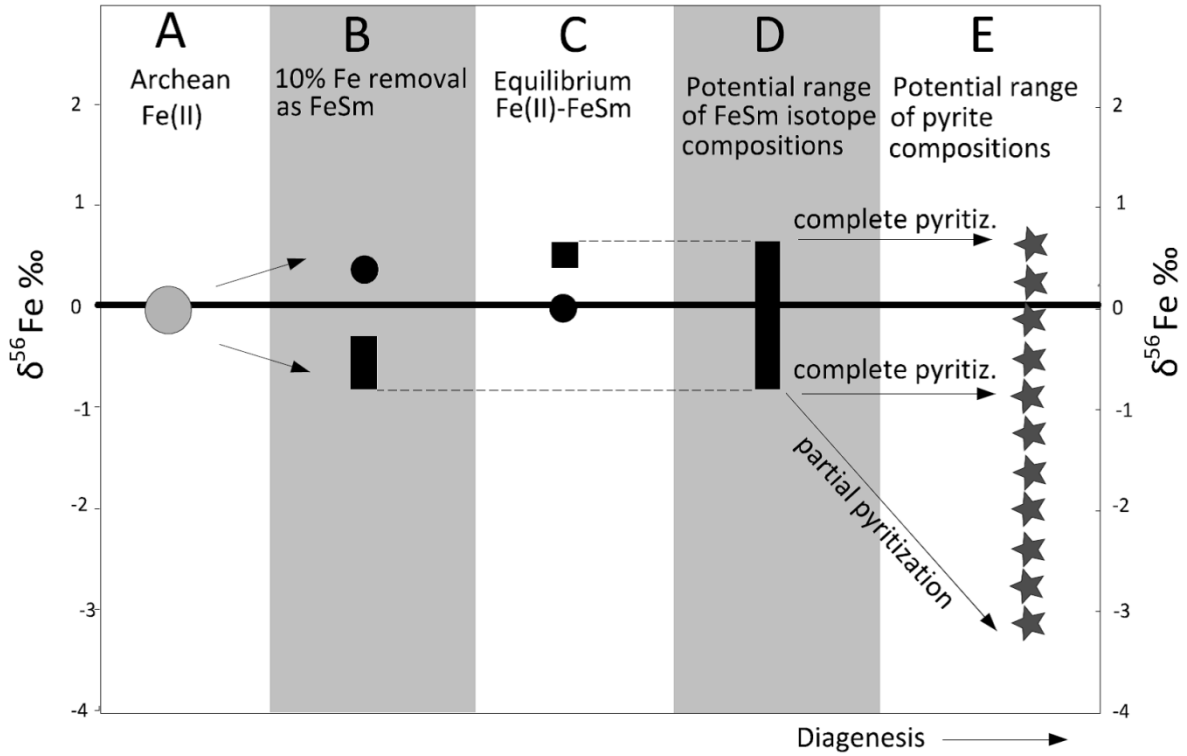

Fig. 2: Schematic diagram representing the abiotic formation of ^{56}Fe depleted pyrite. The light grey circle (column A) represents the isotopic composition of Archean $Fe(II)_{aq}$ seawater *(20)*. Rectangles and black circles represent the isotopic compositions of FeS_m the residual liquid, respectively. Gray stars represent the composition of sedimentary pyrite. The isotopic evolution of iron sulfides during diagenesis is shown during FeS_m precipitation (column B, *(5)*), equilibration with $Fe(II)_{aq}$ (column C, *(21)*) and transfer into pyrite (column E, this study).

The idea that a large ^{56}Fe depleted $Fe(II)_{aq}$ pool in the Archean was required in order to produce depleted pyrite raised the following question: in what sediment is the mass-balancing ^{56}Fe enriched Fe reservoir recorded *(7, 22)*? Although BIFs also display some negative δ^{56}Fe, their mean isotopic composition is ~ 0 to -0.5 ‰ (Fig. 3) *(7)*. Similarly, even though Archean pyrites display $\delta^{56}Fe_{pyrite}$ values down to -3.5 ‰, the isotopic distribution clusters between -1.2 and -2.2 ‰ (Fig. 3). If the pyrite forming mechanism itself is responsible for the observed compositions, Archean pyrite signatures indicate that the Fe isotope composition of the $Fe(II)_{aq}$ reservoir was ~ 0 ‰ and that the degree of Fe(II) utilization was low. In the Archean environment where $Fe(II)_{aq}$ with δ^{56}Fe ~ 0 ‰ is

continually injected into the system by hydrothermal vents, small amounts of Fe removal as pyrite would not dramatically change the isotopic composition of the remaining $Fe(II)_{aq}$ pool and we propose that there is no need for a large ^{56}Fe depleted $Fe(II)_{aq}$ pool to be produced prior to pyrite formation. Certainly, both DIR and the removal of $Fe(II)_{aq}$ as BIFs in ferruginous regions would promote the production of ^{56}Fe depleted fluids enabling the formation of light sedimentary pyrite. However the signatures typically observed in sedimentary pyrite are not diagnostic for DIR. We suggest that low $\delta^{56}Fe$ signatures in Archean sedimentary pyrite indicate that the portion of Fe removed as pyrite was relatively small in respect with the portion of Fe remaining in the Fe(II) pool *(23)*, which should be tested in geological studies against the degree of pyritization *(24)*. We note that a correlation between Fe and S isotope compositions can also be obtained by varying the degree of Fe and S utilization as pyrite.

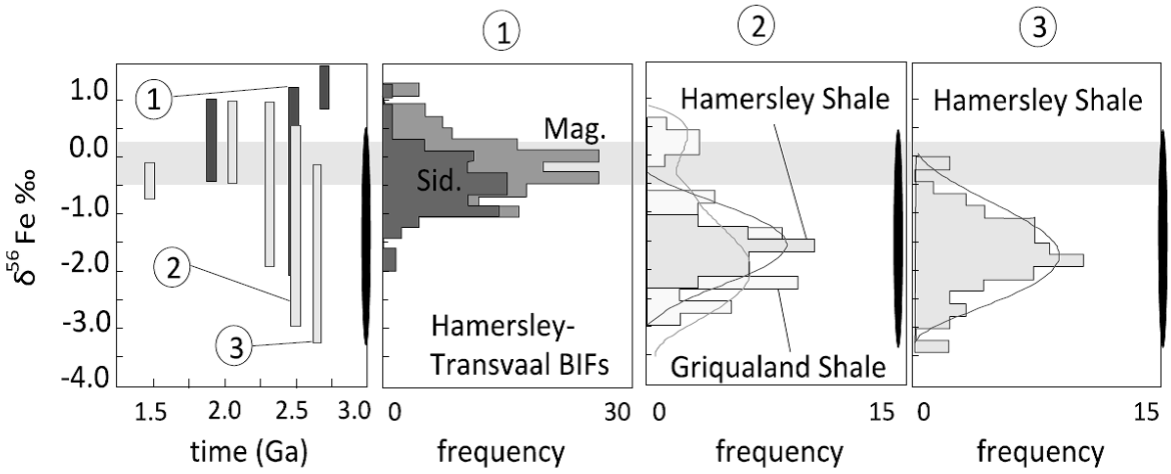

Fig. 3: The Fe isotopic distribution of some Archean BIFs minerals (magnetite and siderite) in the Hemersley and Transvaal Basins (1) and of some Archean sulfidic shales (pyrite and pyrite nodules) in the Hamersley (2 and 3) and Griqualand Basins (2). BIFs data are from *(7)*. Pyrite data are from *(2)*. The mean weighed value is ~ 0 to -0.5 ‰ for BIFs and ~ -1.5 ‰ for Archean sedimentary pyrite. The black areas represent the possible spectrum of pyrite isotope signatures (this study) when pyrite forms from precipitated FeS_m that represents 10 % of the $Fe(II)_{aq}$ reservoir. The grey area represents the composition range between igneous rocks and hydrothermal fluids. Modified after *(7)*.

The rise of the oxygen into the atmosphere would have stimulated bacterial sulfate reduction through the increase sulfate fluxes due to oxidative continental weathering *(25)*. Persistence of euxinic regions throughout the Proterozoic would have enhanced $Fe(II)_{aq}$ removal as sulfides, narrowing down the range of $\delta^{56}Fe_{pyrite}$. In the Proterozoic oceans, strongly stratified with oxic shallow waters, euxinic mid-depth proximal regions and deep, distal ferruginous waters *(24, 26)*, both pyritic black shales and BIFs or their Fe oxide precipitate precursors sequestered $Fe(II)_{aq}$ and BIFs deposition ended in the late Proterozoic. In these oceans in which $Fe(II)_{aq}$ is extensively utilized as pyrite or oxides, $\delta^{56}Fe_{pyrite}$ would progressively reflect the values of the $Fe(II)_{aq}$ source. The 2.3 to ~1.8 Ga period, for which $\delta^{56}Fe_{pyrite}$ displays values up to ~ +1.2 ‰, may suggest major $Fe(II)_{aq}$ source changes in the stratified oceans *(11)*. Where ^{56}Fe enriched Fe(III) bearing (hydr)oxides become a dominant $Fe(II)_{aq}$ source, abiotic dissolution of Fe(III) (hydr)oxides by H_2S produces ^{56}Fe enriched $Fe(II)_{aq}$ *(27)*, and the isotopic composition of the source would be ^{56}Fe enriched. Dissolution of siderite would also contribute to the production of ^{56}Fe enriched $Fe(II)_{aq}$ *(28)*. Close temporal and spatial association of ^{56}Fe enriched pyrite with BIFs *(2)* supports the idea that pyrite formed through the H_2S dissolution of BIFs minerals. Note that theoretical computations predict that at equilibrium pyrite is a heavy phase *(4)*. Under normal sedimentary conditions it is unlikely that pyrite compositions reflect equilibrium due to the extremely low solubility of pyrite, but higher temperature and late diagenetic effects could favor isotope exchange towards equilibrium.

The end of the Proterozoic is characterized by the decrease of $Fe(II)_{aq}$ in oceans and the spatial limitation of anoxic and ferruginous basins. In this context, DIR and H_2S dissolution of Fe(III) (oxy)hydroxides become the major $Fe(II)_{aq}$ source rather than hydrothermal $Fe(II)_{aq}$ inputs. The implication is that where [S(-II)] is not a limiting factor for pyrite formation, pyrite should display $\delta^{56}Fe_{pyrite}$ values approaching those of seawater $Fe(II)_{aq}$. $\delta^{56}Fe_{pyrite}$ data varying from ~ -0.4 to ~ -1.2 ‰ in modern anoxic sediments *(3, 29)* are consistent with the idea that $\delta^{56}Fe_{pyrite}$ signatures reflect

the degree of Fe utilization as pyrite. In modern sediments, where DIR can be extensive *(3)*, pore water $Fe(II)_{aq}$ is ^{56}Fe depleted. However, fractionation factors cannot be directly calculated from the measured Fe isotopic compositions of the natural phases since $Fe(II)_{aq}$ can remain dissolved for large durations and there is no reason why coexisting Fe^{2+}_{aq}, FeS_m and pyrite within a sediment should be cogenetic *(15)*. The production of ^{56}Fe depleted pore water $Fe(II)_{aq}$ is not restricted to DIR but also to Fe partial removal as ^{56}Fe enriched (hydr)oxides and Fe adsorption onto Fe (hydr)oxides *(30)*. In some modern sediments, where polysulfide becomes an important $S(-II)_{aq}$ species, the pyrite forming mechanism may be different to those evaluated here, and therefore may be accompanied by a different fractionation.

References and notes

1. A. Matthews et al., *Geochimica et Cosmochimica Acta* 68, 3107-3123 (2004).

2. O. J. Rouxel, A. Bekker, K. J. Edwards, *Science* 307, 1088-1090 (2005).

3. S. Severmann, C. M. Johnson, B. L. Beard, J. McManus, *Geochim Cosmochim Acta* 70, 2006–2022 (2006).

4. V. B. Polyakov, R. N. Clayton, J. Horita, S. D. Mineev, *Geochimica et Cosmochimica Acta* 71, 3833-3846 (2007).

5. I. B. Butler, C. Archer, D. Vance, A. Oldroyd, D. Rickard, *Earth and Planet. Science Letters* 236 (2005).

6. Y. Duan et al., *Earth and Planetary Science Letters* 290, 244-253 (2010).

7. C. M. Johnson, B. L. Beard, E. E. Roden, *Annual Review of Earth and Planetary Sciences* 36, 457-493 (2008).

8. C. Archer, D. Vance, *Geology* 34, 153-156 (2006).

9. R. Raiswell, D. E. Canfield, *Am J Sci* 298, 219-245 (1998).

10. J. L. Skulan, B. L. Beard, C. M. Johnson, *Geochim. Cosmochim. Acta* 66, 2995-3015 (2002).

11. A. D. Anbar, O. Rouxel, *Annu. Rev. Earth Planet. Sci.* 35, 717–746 (2007).

12. Materials and methods and results are available as supporting material on Science Online.

13. D. Rickard, G. W. Luther, *Geochim. Cosmochim. Acta* 61, 135–147 (1997).

14. G. W. Luther, D. Rickard, *Journal of Nanoparticle Research* 7, 389-407 (2005).

15. D. Rickard, G. W. Luther, *Chem. Rev.* 107, 514-562 (2007).

16. E. A. Schauble, *Reviews in Mineralogy & Geochemistry* 55, 65-111 (2004).

17. A. D. Anbar, J. E. Roe, J. Barling, K. H. Nealson, *Science* 288, 126-128 (2000).

18. I. B. Butler, M. E. Bottcher, D. Rickard, A. Oldroyd, *Earth and Planet. Science Letters* 228, 495-509 (2004).

19. A. E. Isley, *The Journal of Geology* 103, 169-185 (1995).

20. K. E. Yamaguchi, C. M. Johnson, B. L. Beard, H. Ohmoto, *Chem. Geol.* 218, 135-169 (2005).

21. R. Guilbaud, I. B. Butler, R. M. Ellam, D. Rickard, A. Oldroyd, *Geochimica et Cosmochimica Acta* 75, 2721-2734 (2011).

22. A. D. Czaja et al., *Earth and Planetary Science Letters* 292, 170-180 (2010).

23. D. E. Canfield, *Annual Review of Earth and Planetary Sciences* 33, 1-36 (2005).

24. S. W. Poulton, P. W. Fralick, D. E. Canfield, *Nature Geosci* 3, 486-490 (2010).

25. D. E. Canfield, *Nature* 396, 450-453 (1998).

26. C. Li et al., *Science* 328, 80 -83 (2010).

27. A. McAnena, S. Severmann, S. W. Poulton, *Goldschmidt Conference Abstracts* (2009).

28. C. M. Johnson, E. E. Roden, S. A. Welch, B. L. Beard, *Geochimica et Cosmochimica Acta* 69, 963-993 (2005).

29. S. Severmann et al., *Geology* 36, 487-490 (2008).

30. O. J. Rouxel, M. Auro, *Geostandards and Geoanalytical Research* 34, 135-144 (2010).

References from SOM

31. I. Butler, M. Schoonen, D. Rickard, *Talanta* 41, 211-215 (1994).

32. D. Rickard et al., *Chem. Geol.* 235 (2006).

33. A. Kandegedara, D. B. Rorabacher, *Analytical Chemistry* 71, 3140-3144 (1999).

34. A. Zehnder, K. Wuhrmann, *Science* 194, 1165-1166 (1976).

35. I. Butler, D. Rickard, *Geochim Cosmochim Acta* 64, 2665–2672 (2000).

36. E. Drobner, H. Huber, G. Wächtershäuser, D. Rose, K. Stetter, *Nature* 346, 742-744 (1990).

37. M. A. Huerta-Diaz, J. W. Morse, *Marine Chemistry* 29, 119-144 (1990).

38. A. Vogel, *Longmans, Green and Co.* (1951).

39. R. Guilbaud, R. Ellam, I. Butler, V. Gallagher, K. Keefe, *J. Anal. At. Spectrom* 25, 1598-1604 (2010).

40. R. Criss, *Oxford University Press, New York* , 244pp (1999).

41. D. Rickard, *Geochimica et Cosmochimica Acta* 70, 5779-5789 (2006).

Acknowledgements

This work was funded by an ECOSSE PhD studentship to RG and NERC research grant NE/E003958/1 to IBB. We are thankful to K. Keefe, V. Gallagher, N. Odling, B.D. Roach, S. Mowbray and C. Fricke for technical support. We also thank B. Ngwenya, A. Matthews, D. Rickard, A. McAnena and M. Pękala for constructive discussions.

Supporting Online Material

Experimental methods

All reagents were of analytical grade and solutions were prepared using 17-18 MΩcm deionised water, sparged with O_2-free grade N_2 for 30 min (*31*). FeS_m synthesis and the preparation of solutions were performed under O_2 free conditions in a N_2-filled re-circulating Saffron alpha® anoxic chamber. Iron solutions were made by dissolution of Mohr's salt $Fe(NH_4)(SO_4).6H_2O$ (Sigma Aldrich™) in N_2 sparged water. Mohr's salt was used for its ability to resist oxidation. Sulphide solutions were made by dissolution of $Na_2S.9H_2O$ (Sigma Aldrich™) in N_2 sparged water. FeS_m was precipitated mixing 100 mL 0.6 M $Na_2S.9H_2O$ solution with 100 mL 0.6 M $(NH_4)_2Fe(SO_4)_2$ solution (*13*). The precipitate was filtered with a Buchner filter (Whatman™ No. 1 paper) and the filtrate was filtered with a 0.45 µm membrane Millipore™ filter. Freshly precipitated FeS_m was re-suspended in water and re-filtered three times, freeze-dried for three days on a Mini-Lyotrap (LTE®) freeze-dryer and stored in the glove-box (*32*). The non-metal complexing buffer (*33*) (3-N-morpholinopropanesulfonic acid, p*K*a = 7.31, Fisher™) was made by dissolution of its sodium salt and buffered to pH 6 by NaOH titration. Ti(III) citrate was prepared adding 5 mL 15% $TiCl_3$ to 50 mL 0.2 M Na citrate and buffered to pH 7 with Na_2CO_3 (*13, 34*).

In the glove box, 0.005 mol of freeze-dried FeS_m was introduced into a reaction-vessel and 10 mL of a 0.05 M MOPS (pH 6) buffer were added. The reaction-vessel was either a heat-sealed glass ampoule (*13, 35, 19*, in the case of the "Py" experiments) or a rubber sealed serum bottle (*35, 36,* in the case of the "SB" experiments). Sealed reaction-vessels were closed and attached to a gas-transfer manifold (*13*). The manifold was flushed with O_2-free grade N_2 and pumped down to ~ -14 PSI (~ -97 kPa, full vacuum) three times. A serum bottle containing a weighed amount of $Na_2S.9H_2O$ was attached to the manifold with a hypodermic needle and 50% v/v N_2 sparged H_2SO_4 was injected into the serum bottle *via* a syringe to generate H_2S. After H_2S transfer into the reaction-vessel, the pressure was adjusted to slight under-pressure (~ -2.5 PSI or ~ -17 kPa) to ensure the sealing of the vessel using a glassblower's torch (for Py experiments). Excess H_2S was pumped out to waste. The sealed reaction-vessel was kept at constant temperature in a 100°C furnace or in a 40°C water bath. Vessels were allowed different durations of reaction, and frozen to stop the reaction for pending mineral extraction.

Once frozen, the reaction-vessel was opened, flushed with N_2 to remove the excess of H_2S from the head-space, and attached to a freeze-dryer for three days. In the glove-box, ~ 0.1 g of the solids,

i.e. a mixture of mackinawite, pyrite and MOPS salts, was loaded and sealed onto the metal (Al) support of an environmental sample holder for immediate XRD characterisation (*16*). A small portion of the solids were carbon coated for immediate SEM analysis. Separation between pyrite and mackinawite from the remaining solids was completed using modified preferential dissolution of existing protocols (*4, 37*). Solids (0.1 g) were introduced into a serum bottle along with 2 mL H_2O and a few drops of Ti(III) citrate. Ti(III) citrates ensures the complete dissolution of FeS_m in HCl, avoiding the formation of insoluble S(0) by poising Eh to low negative values (*32*). Ti(III) is not sufficiently reducing to encourage the dissolution of pyrite. Rickard *et al.* (*32*) performed FeS_m digestion in hot 1.2 M or 6 M HCl and 5 mL Ti(III) citrate. Our aim was to maximise quantitative FeS_m dissolution with minimum Fe input from Ti(III) citrate and from FeS_2 partial dissolution. Best results were obtained by adding a few drops Ti(III) citrate to FeS_m in 1.2 M HCl. This volume decreases the input of Fe from Ti(III) citrate to < 0.7 % of Fe brought by FeS_m when FeS_m constitutes 5 % of total Fe. In other words, even for the lowest FeS_m concentrations, $Fe_{Ti(III)citrate}$ is still negligible compared to Fe_{FeSm}, and has no impact on the measured isotopic compositions. In a fume cupboard, 20 mL 1.2 M purged HCl was injected into the serum bottle *via* a hypodermic syringe in order to dissolve only FeS_m and the MOPS salts. Remaining solids, essentially pyrite, were separated from solution on a 0.45 µm membrane Millipore™ filter and dissolved with a few drops of concentrated HNO_3. No solids passed the filter. Potential partial dissolution of pyrite into the Fe_{FeS} solution and its consequences are discussed later. Both Fe_{pyrite} and Fe_{FeS} solutions were taken to dryness, treated with H_2O_2 for quantitative removal of the carbon-salts left by MOPS. During this process, Ti from Ti(III) citrate precipitated as insoluble Ti-oxides that were removed by filtration. Fe solutions were dissolved in *aqua regia*, evaporated and re-dissolved in 5 % HNO_3 for pending [Fe] determination and Fe isotope ratios analysis.

Analytical methods

We tested the determination of the pyrite percentage (%Py) from the high peak area (around 16° 2θ for mackinawite, and around 32° 2θ for pyrite) with standard mackinawite-pyrite mixtures. Freeze-dried mackinawite was prepared as described above. Natural pyrite was ground with a McCrone® mill for 12 min down to a mean diameter of 4 µm (analysed on a Beckman Coulter LS® particle size analyser). Typical mixtures were 0, 20, 30, 50, 60, 70, 80, 85 and 100 wt%Py. About 0.1 g of the sample was loaded onto a metal environmental sample holder. The environmental holder containing the sample was loaded on a Bruker D8 Advance® Diffractometer. XRD analysis was performed using Cu*K*α primary radiation generated at an accelerating voltage of 40KV in the range of 2-65° 2θ with a 1s/0.02° 2θ counting time. The diffracted X-rays were recorded by a Sol-x™ energy

dispersive detector. Data were filtered to remove Cu*K*αII peaks. Peak areas for mackinawite and pyrite respond linearly to the weighted %Py from the standard mixtures. Precision on %Py calculated from the peak areas is given by replicates measurements of the calibration mixture and is ± 7 % (2σ level). Measuring the peak areas for mackinawite and pyrite in our samples thus allowed us to determine a degree of pyritisation. The MOPS salts did not show any peak on the XRD spectra and did not perturb the standard response.

Total Fe concentrations in Fe_{FeS} and Fe_{pyrite} solutions were determined in order to confirm the extent of pyritisation given by the XRD scans. We used the thiocyanate method (*38*) to determine [Fe(III)] in the solutions by comparison with a calibration curve. Fe solutions were acidified with 2 mL 1:5 HNO_3, oxidised with a few drops of 0.2 M potassium permanganate, reacted with 5 mL 4 M potassium thiocyanate and made up to 50 mL. [Fe(III)] analysis was performed on a M501 single beam spectrophotometer (Spectronic Analytical Instruments®) using a wavelength of 480 µm. The Beer-Lambert's law is followed for a 0 to 5 ppm [Fe(III)] range with a precision 2σ = ± 0.1 ppm. Table S1 compares the relative %Py obtained with [Fe(III)] analysis and with XRD analysis.

Sample imaging, mineral products determination and texture description were performed *via* backscatter detector on a Philips XL30CP® Scanning Electron Microscope (SEM) at 20 kV. Qualitative chemical analysis on the material surface was carried out with PGT® Spirit X-ray analysis as a mineralogical check.

Fe isotope analysis has been described in detail elsewhere (*39*). Samples (Fe(III) in HCl) were taken to dryness and re-dissolved in 5% HNO_3. No column chemistry was performed since our samples were experimentally synthesised from analytical grade reagents. $^{56/54}$Fe and $^{57/54}$Fe isotope ratios were measured on a GV IsoProbe (formerly Micromass) multi-collection inductively coupled mass spectrometer (MC-ICP-MS). The major challenge for accurate and precise measurement of Fe isotopes is the removal of atomic and polyatomic interferences induced by the Ar plasma. This was achieved by increasing the signal-to-background ratio (using high concentration samples and introducing collision gases into the hexapole to decrease and/or remove the interferences) and by stabilising the instrumental mass bias minimising the hexapole potential and decreasing the extraction voltage. 3-10 ppm Fe solutions were introduced into an ApexQ inlet system at 50 µL.min^{-1} to maximise the signal to ~0.3 V on mass 54, ~6 V on mass 56 and ~0.02 V on mass 57. Hexapole rf amplitude was set at 50% which enhances transmission of Fe masses. The analysis was run in hard extraction mode (-250 V). 1.8 mL min^{-1} Ar and 2 mL min^{-1} H_2 were introduced into the hexapole collision cell to completely remove ArN^+ on mass 54 and $ArOH^+$ on mass 57 and to decrease ArO^+ on

mass 56 to 0.006 V which represents 0.1% of the Fe peak. Cr^+ interferences on mass 54 were monitored on mass 52 but never detected. Instrumental mass bias was corrected by bracketing each sample with a standard and Fe isotope results are presented conventionally using the $\delta^{56}Fe$ and $\delta^{57}Fe$ notations in ‰ IRMM-014:

$$\delta^{56}Fe = \left(\frac{(^{56}Fe/^{54}Fe)sample}{(^{56}Fe/^{54}Fe)IRMM} - 1 \right) \times 10^3$$

$$\delta^{57}Fe = \left(\frac{(^{57}Fe/^{54}Fe)sample}{(^{57}Fe/^{54}Fe)IRMM} - 1 \right) \times 10^3$$

The precision of our measurements was the reproducibility 2sd for the sample set described in this manuscript, obtained by measuring an external standard and was ± 0.08 ‰ and ± 0.16 ‰ (2σ) for $\delta^{56}Fe$ and $\delta^{57}Fe$ respectively.

Modelling approach

Models for the isotopic evolution of the FeS_m-FeS^0_{aq}-pyrite system at 40°C and 100°C have been calculated in Matlab 7.7.0 (MathWorks®). If we consider a system in which phase A (here $Fe(II)_{RES}$ = FeS_m + FeS^0_{aq}) incrementally transfers into phase B (pyrite) with the Fe isotope fractionation $\Delta^{56}Fe_{Fe(II)RES\text{-}pyrite}$ without any further exchange between A and B, the isotopic evolution of the system is described by the incremental Rayleigh equation (*40*):

$$\frac{1000 + \delta^{56}_{Fe(II)RES_t}}{1000 + \delta^{56}_{Fe(II)RES_{initial}}} = f^{\alpha_{pyrite-Fe(II)RES}-1}$$

where *f* is the fraction of $Fe(II)_{RES}$ remaining in the system at each time *t*, and *α* stands for the fractionation factor between pyrite and $Fe(II)_{RES}$. This simple Rayleigh fractionation has been applied to the 40°C data, but is not a close fit to the 100°C data.

For the 100°C data, we considered the fact that only FeS^0_{aq} transfers into pyrite with the $\Delta^{56}Fe_{FeS(0)aq\text{-}pyrite}$ fractionation, and that at this temperature the remaining ^{56}Fe enriched FeS^0_{aq} can homogenise with FeS_m. The isotopic evolution of each phase is calculated for three steps: i) the dissolution of FeS_m into FeS^0_{aq}, ii) the ^{56}Fe depleted pyrite forming reaction from FeS^0_{aq} and iii) the isotopic homogenisation between FeS_m and ^{56}Fe enriched FeS^0_{aq}.

i) FeS_m dissolution step

In this step pyrite is not formed yet, and we assume that there is no Fe isotope fractionation involved during the dissolution of FeS_m into FeS^0_{aq}. If *q* is the amount of FeS_m dissolved into FeS^0_{aq}, the concentration at every time of both phases is given by:

$$C_{FeSm}^{i+1} = C_{FeSm}^{i} - q,$$

$$C_{FeS(0)aq}^{i+1} = C_{FeS(0)aq}^{i} + q, \text{ and}$$

$$C_{Pyrite}^{i+1} = C_{Pyrite}^{i}.$$

The isotopic composition of each phase is given by:

$$\delta_{FeSm}^{i+1} = \frac{C_{FeSm}^{i}\delta_{FeSm}^{i} - q\delta_{FeSm}^{i}}{C_{FeSm}^{i+1}} = \delta_{FeSm}^{i},$$

$$\delta_{FeS(0)aq}^{i+1} = \frac{C_{FeS(0)aq}^{i}\delta_{FeS(0)aq}^{i} + q\delta_{FeSm}^{i}}{C_{FeS(0)aq}^{i+1}} = \frac{C_{FeS(0)aq}^{i}\delta_{FeS(0)aq}^{i} + q\delta_{FeSm}^{i}}{C_{FeS(0)aq}^{i} + q}, \text{ and}$$

$$\delta_{Pyrite}^{i+1} = \delta_{Pyrite}^{i}.$$

ii) Pyrite forming step

In this step, FeS_m is unchanged, whereas *z* amount of FeS^0_{aq} is transferred into pyrite with an isotope fractionation *F*. The concentration of each phase is given by:

$$C_{FeSm}^{i+2} = C_{FeSm}^{i+1} = C_{FeSm}^{i} - q,$$

$$C_{FeS(0)aq}^{i+2} = C_{FeS(0)aq}^{i+1} - z = C_{FeS(0)aq}^{i} + q - z, \text{ and}$$

$$C_{Pyrite}^{i+2} = C_{Pyrite}^{i+1} = C_{Pyrite}^{i} + z.$$

The isotopic composition of each phase is given by:

$$\delta_{FeSm}^{i+2} = \delta_{FeSm}^{i+1} = \delta_{FeSm}^{i},$$

$$\delta_{FeS(0)aq}^{i+2} = \frac{C_{FeS(0)aq}^{i+1}\delta_{FeS(0)aq}^{i+1} - z\left(\delta_{Fe(0)aq}^{i+1} - F\right)}{C_{FeS(0)aq}^{i+2}}$$

$$= \frac{\left(C_{FeS(0)aq}^{i} + q\right)\left(\frac{C_{FeS(0)aq}^{i}\delta_{FeS(0)aq}^{i} + q\delta_{FeSm}^{i}}{C_{FeS(0)aq}^{i} + q}\right) - z\left(\frac{C_{FeS(0)aq}^{i}\delta_{FeS(0)aq}^{i} + q\delta_{FeSm}^{i}}{C_{FeS(0)aq}^{i} + q} - F\right)}{C_{FeS(0)aq}^{i} + q - z}$$

$$= \frac{\left(C_{FeS(0)aq}^{i}\delta_{FeS(0)aq}^{i} + q\delta_{FeSm}^{i}\right) - z\left(\frac{C_{FeS(0)aq}^{i}\delta_{FeS(0)aq}^{i} + q\delta_{FeSm}^{i}}{C_{FeS(0)aq}^{i} + q} - F\right)}{C_{FeS(0)aq}^{i} + q - z}$$

$$\delta_{Pyrite}^{i+2} = \frac{C_{Pyrite}^{i}\delta_{Pyrite}^{i} + z\left(\delta_{Fe(0)m}^{i+1} - F\right)}{C_{Pyrite}^{i+2}}$$

$$= \frac{C_{Pyrite}^{i}\delta_{Pyrite}^{i} + z\left(\frac{C_{FeS(0)aq}^{i}\delta_{FeS(0)aq}^{i} + q\delta_{FeSm}^{i}}{C_{FeS(0)aq}^{i} + q} - F\right)}{C_{Pyrite}^{i} + z}$$

iii) Homogenisation of the Fe(II) reservoir

In this step, pyrite is unchanged, whereas FeS_m and FeS^0_{aq} exchange and homogenise (still assuming that there is no isotope fractionation between FeS_m and FeS^0_{aq}). The isotopic composition of the reservoir is given by:

$$\delta_{FeS(0)aq}^{i+3} = \delta_{FeSm}^{i+3} = \frac{C_{FeS(0)aq}^{i+2}\delta_{FeS(0)aq}^{i+2} + C_{FeSm}^{i+2}\delta_{FeSm}^{i+2}}{C_{FeS(0)aq}^{i+3} + C_{FeSm}^{i+3}}$$

$$\delta_{FeS(0)aq}^{i+3} = \delta_{FeSm}^{i+3} = \frac{\left(C_{FeS(0)aq}^{i} + q - z\right)\frac{\left(C_{FeS(0)aq}^{i}\delta_{FeS(0)aq}^{i} + q\delta_{FeSm}^{i}\right) - z\left(\frac{C_{FeS(0)aq}^{i}\delta_{FeS(0)aq}^{i} + q\delta_{FeSm}^{i}}{C_{FeS(0)aq}^{i} + q} - F\right)}{C_{FeS(0)aq}^{i} + q - z} + \left(C_{FeSm}^{i} - q\right)\delta_{FeSm}^{i}}{C_{FeS(0)aq}^{i} + C_{FeSm}^{i} - z}$$

$$\delta_{FeS(0)aq}^{i+3} = \delta_{FeSm}^{i+3} = \frac{\left(C_{FeS(0)aq}^{i}\delta_{FeS(0)aq}^{i} + q\delta_{FeSm}^{i}\right) - z\left(\frac{C_{FeS(0)aq}^{i}\delta_{FeS(0)aq}^{i} + q\delta_{FeSm}^{i}}{C_{FeS(0)aq}^{i} + q} - F\right) + \left(C_{FeSm}^{i} - q\right)\delta_{FeSm}^{i}}{C_{FeS(0)aq}^{i} + C_{FeSm}^{i} - z}$$

The three steps mentioned above were calculated until complete consumption of the Fe(II) reservoir. We used the FeS_m solubility data from Rickard (*41*) to determine the concentration of

FeS^0_{aq}. In order to keep the concentration of FeS^0_{aq} constant, we set equal values for *q* and *z*, *i.e.* we assume that dissolution of FeS_m to FeS^0_{aq} is equal or faster than consumption of FeS^0_{aq} to form FeS_2.

Results and discussion for the separation procedure

Experimental results are summarised in Table S1. For all experiments, final products were pyrite and mackinawite. No Fe(II) oxidation happened during reaction. The use of hermetically sealed glass ampoules or serum bottles gave identical Fe isotope results. The only effect we could identify using different reaction vessels was the rate of pyrite formation. Initial $\delta^{56}Fe_{FeSm}$ was 0.30 ± 0.08 ‰ Isotopic mass balance for each experiment (0.29 ± 0.09 ‰) indicates that the experimental error is small and our results are reproducible. A three-isotope plot (Fig. S1) supports the quality of our data points which are consistent with Fe isotope fractionation along the terrestrial mass fractionation line. Our data highlight the large fractionation occurring during pyrite formation with FeS_m and H_2S as reactants. Final precision on the extent of pyritisation (%Py) is ± 10 %.

The risk of Fe_{pyrite} contamination during FeS_m dissolution with HCl was examined. This risk is enhanced when the ratio FeS_m/FeS_2 decreases. We used cold 1.2 M HCl rather than 6 M HCl in order to reduce FeS_2 dissolution and measured a maximum of 0.2 % dissolution from the initial FeS_2 phase. This means that when the FeS_m/FeS_2 ratio is the lowest, potential pollution of Fe_{FeSm} by Fe_{pyrite} represents at maximum 0.027 % of Fe_{FeSm}. Note that such contamination would shift by 0.1 ‰ the composition of observed FeS_m only for degrees of pyritisation > 95 % (*i.e.* when < 5 % FeS_m remains in the system). None of our data correspond to this high %Py region, and we are confident that our results are free from cross-contamination.

Removal of organic matter left by MOPS after freeze-drying was crucial to prevent carbon to be introduced into the MC-ICP-MS. Both *aqua regia* and hydrogen peroxide (VWR™) were tested to oxidatively remove organic carbon. 5 to 10 mL of the oxidant was added to the residue and warmed up to 85°C and dried. The procedure was repeated three times. The final residue was dissolved in concentrated HCl and taken up to volume. 5 µL of the solutions were diluted four times in methanol for Electron Spray Ionisation Mass Spectrometry (ESI-MS). Results showed that MOPS is still present in the solution oxidised with *aqua regia* whereas MOPS is not detectable in the solution oxidised with hydrogen peroxide. NMR analysis showed the persistence of organic molecules in both solutions, but peaks were broad and difficult to analyse, perhaps indicating sulphur and nitrogen containing molecules. Total Organic Carbon (TOC) analyses showed that 99 % of carbon had been removed from the solution oxidised with hydrogen peroxide.

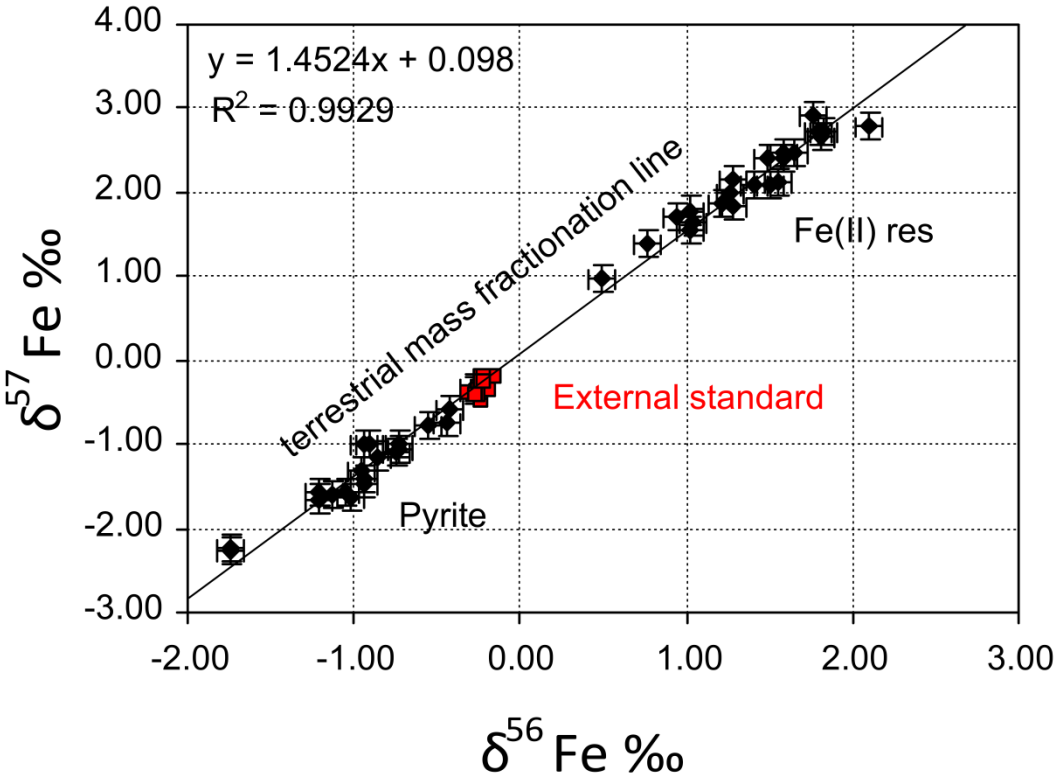

Fig. S1.

Analytical quality control for all experimental samples including the Baker Fe solution (external standard, in red) normalized with IRMM-14 in a three isotope plot. The slope of the line is consistent with the terrestrial mass fractionation line.

Table S1.

Experimental conditions and analytical results. Precision on %Py is ± 10 %. Products were identified by XRD and SEM analyses. Analytical precision on δ^{56}Fe was given by the reproducibility of an external standard (Baker®) at a 2σ level and was ± 0.08 ‰ and ± 0.16 ‰ for δ^{56}Fe and δ^{57}Fe respectively. The isotopic composition of starting FeS_m was 0.30 ± 0.08 ‰. The kinetic fractionation factors between FeS_m and pyrite, $\alpha'_{FeS\text{-}pyrite}$ was given by $\alpha'_{FeS-pyrite} = \frac{1000 + \delta^{56}Fe_{FeS}}{1000 + \delta^{56}Fe_{FeS}}$. Precision on $\alpha'_{FeS\text{-}pyrite}$ is ± 0.0007. The fractionation between FeS_m and pyrite was $\Delta^{56}Fe_{FeS-pyrite} = \delta^{56}Fe_{FeS} - \delta^{56}Fe_{pyrite}$ and was given with a precision of ± 0.11 ‰.

Samples	T °C	Duration (hours)	Products	% Py spectr.	% Py XRD	FeSm $\delta^{56}Fe$ (‰)	FeSm $\delta^{57}Fe$ (‰)	Pyrite $\delta^{56}Fe$ (‰)	Pyrite $\delta^{57}Fe$ (‰)	$\alpha'_{FeS\text{-}pyrite}$	$\Delta^{56}Fe_{FeS\text{-}pyrite}$	mass balance $\delta^{56}Fe$ = 0.3 ‰	Baker external standard $\delta^{56}Fe$ (‰)	Baker external standard $\delta^{57}Fe$ (‰)
SB-1HA	100	3	py, mk	0.33	0.34	0.94	1.71	-0.72	-1.05	1.0017	1.66	0.37	-0.25	-0.40
SB-1HB	100	3	py, mk	0.38	0.45	1.03	1.55	-0.74	-1.08	1.0018	1.77	0.23	-0.21	-0.36
SB-1DA	100	17.5	py, mk	0.34	0.26	0.77	1.38	-1.13	-1.59	1.0019	1.89	0.27	-0.26	-0.42
SB-1DB	100	19.5	py, mk	0.40	0.4	1.21	1.86	-1.05	-1.58	1.0023	2.25	0.31	-0.15	-0.19
SB-2DA	100	48	py, mk	0.32	0.39	1.04	1.64	-0.93	-1.47	1.0020	1.98	0.27	-0.23	-0.19
SB-2DB	100	48	py, mk	0.43	0.37	1.03	1.79	-0.95	-1.33	1.0020	1.98	0.30	-0.21	-0.27
SB-3DB	100	72	py, mk	0.41	0.43	1.28	2.16	-0.95	-1.31	1.0022	2.23	0.32	-0.25	-0.33
Py1DE	100	24	py, mk	0.75	0.64	1.49	2.41	-0.44	-0.75	1.0019	1.93	0.25	-0.23	-0.50
Py2DC	100	48	py, mk	0.80	0.74	1.80	2.74	-0.28	-0.36	1.0021	2.08	0.26	-0.25	-0.34
PyA1	100	122	py, mk	0.70	0.71	1.81	2.66	-0.28	-0.32	1.0021	2.10	0.33	-0.21	-0.19
PyA2	100	25	py, mk	0.58	0.59	1.58	2.46	-0.55	-0.76	1.0021	2.13	0.32	-0.30	-0.38
PyA3	100	5.5	py, mk	0.56	0.56	1.40	2.10	-0.72	-0.99	1.0021	2.13	0.21	-0.25	-0.42
PyA4	100	50	py, mk	0.69	0.68	1.83	2.73	-0.42	-0.60	1.0023	2.25	0.30	-0.21	-0.30
PyA5	100	1.5	py, mk	0.50	0.48	1.55	2.11	-1.03	-1.62	1.0026	2.57	0.31	-0.22	-0.29
													-0.23	-0.40
SB-5HA	40	5	py, mk	0.33	0.46	1.59	2.42	-1.22	-1.65	1.0028	2.80	0.30	-0.25	-0.38
SB-5HB	40	5	py, mk	0.55	0.5	1.76	2.90	-1.21	-1.56	1.0030	2.97	0.27	-0.24	-0.38
SB-1DC	40	24	py, mk	0.62	0.53	1.64	2.47	-0.93	-1.40	1.0026	2.58	0.28	-0.19	-0.35
SB-2DC	40	48	py, mk	0.46	0.45	1.50	2.10	-0.90	-1.00	1.0024	2.40	0.42	-0.25	-0.37
SB-2DD	40	48	py, mk	0.48	0.6	2.10	2.80	-0.94	-0.98	1.0030	3.04	0.28	-0.24	-0.42
PyA6	40	122	py, mk	0.31	0.48	1.26	1.98	-0.86	-1.14	1.0021	2.11	0.24	-0.24	-0.26
PyA7	40	25	py, mk	0.32	0.32	1.28	1.83	-1.75	-2.26	1.0030	3.02	0.31	-0.21	-0.27
PyA8	40	5.5	py, mk	0.15	0.1	0.49	0.97	-1.75	-2.25	1.0022	2.25	0.27	-0.27	-0.42